Dynamic evolution process of multilayer core-shell microstructures within containerlessly solidifying $Fe_{50}Sn_{50}$ immiscible alloy

W. L. Wang, Y. H. Wu, L. H. Li, D. L. Geng, and B. Wei*
MOE Key Laboratory of Space Applied Physics and Chemistry, Northwestern Polytechnical University, Xi'an 710072, People's Republic of China
(Received 16 August 2015; published 7 March 2016)

Multilayer core-shell structures are frequently formed in polymers and alloys when temperature and concentration fields are well symmetrical spatially. Here we report that two- to five-layer core-shell microstructures were the dominant structural morphology of a binary $Fe_{50}Sn_{50}$ immiscible alloy solidified under the containerless and microgravity states within a drop tube. Three dimensional phase field simulation reveals that both the uniformly dispersive structure and the multilayer core-shells are the various metastable and transitional states of the liquid phase separation process. Only the two-layer core-shell is the most stable microstructure with the lowest chemical potential. Because of the suppression of Stokes motion, solutal Marangoni migration becomes important to drive the evolution of core-shell structures.

DOI: 10.1103/PhysRevE.93.032603

I. INTRODUCTION

Phase separation takes place in various immiscible condensed matter systems, such as polymers, inorganic materials, and metallic alloys, leading to the formation of either homogeneous dispersions or segregated microstructures [1–6]. Besides, some peritectic alloy systems with large positive mixing enthalpy also exhibit metastable phase separation if undercooled sufficiently away from equilibrium states [7–10]. Among the numerous macrosegregation patterns evolving from phase separation, the core-shell structures have attracted great research interest owing to their potential applications [11–14]. Since the microgravity condition facilitates the establishment of spatially symmetrical temperature and concentration fields, the ground simulated space environment, such as the freely falling experiments, inside a drop tube is often applied to investigate the evolution process of core-shell structures [5,15,16]. Meanwhile, the phase field theory provides an effective method to simulate the dynamic mechanisms of core-shell formation through the migration and coagulation of small globules produced by phase separation [7–20]. Because the Stokes motion driven by the density difference of separated phase is suppressed to a considerable extent, the Marangoni migration of globules driven by the temperature and concentration gradients becomes a dominant factor for the phase separation process under a microgravity state [21,22].

A binary $Fe_{50}Sn_{50}$ immiscible alloy that holds such a special composition is located at the crest of the miscibility gap as shown in the Fe-Sn phase diagram of Fig. 1. Thus it possesses a very broad temperature range of 375 K for liquid phase separation. On the other hand, the two separated liquid phases may have comparable weight fractions. Therefore, it offers a desirable model alloy to explore the evolution dynamics of core-shell structures. The objective of this paper is to investigate the rapid solidification mechanisms of immiscible alloys under the microgravity condition within a drop tube. In addition to a systematic study by experiments, three dimensional (3D) phase field simulations are also carried out to visualize the dynamic process of liquid phase separation. Meanwhile, fluid dynamics effects are taken into account to shed further light on the rapid solidification kinetics.

II. EXPERIMENTAL PROCEDURE

The experiments were performed in a 3 m drop tube, which provided a reduced gravity state for 0.78 s. The alloy was prepared from high purity elements of 99.99% Fe and 99.999% Sn in a high vacuum arc-melting furnace. Each sample had a mass of 4 g and was placed in a 13 mm inner diameter $\times$ 15 mm outer diameter $\times$ 160 mm quartz tube, which had a small orifice about 0.3 mm in diameter at the bottom and was installed on the top of the drop tube. The drop tube was then evacuated to 2×10^{-4} Pa and backfilled with a gas mixture of He (99.995%) and Ar (99.999%) to 1×10^{5} Pa. The superheating to 100–150 K above the liquidus temperature was accomplished by induction heating. After that, the bulk sample was dispersed into small droplets by high pressure Ar jetting gas, which fell down freely. The finally solidified samples were polished and etched with a solution of 1 ml hydrogen fluoride +1 ml HNO_3 + 20 ml CH_3CH_2OH + 2 ml H_2O_2. Their solidification structures and solute distribution profiles were investigated with a FEI Sirion electron microscope and an INCA Energy 300 energy dispersive spectrometer (EDS).

III. RESULTS AND DISCUSSION

A. Microstructures formed by containerless solidification

According to the equilibrium Fe-Sn phase diagram [23], the binary $Fe_{50}Sn_{50}$ alloy is located at the peak point of the phase separation zone as shown in Fig. 1. Its liquidus temperature was 1778 K, and the temperature interval of the phase separation reached 375 K. Obviously, the binary $Fe_{50}Sn_{50}$ alloy has a broad immiscible temperature range. In the cooling process, the homogeneous alloy melt was separated into two liquid phases at temperatures below 1778 K: One was an Fe-rich liquid phase, the other was a Sn-rich liquid phase, and the two liquid phases have enough time and temperature intervals to collide and coagulate, which may form the special structure.

*Corresponding author: bbwei@nwpu.edu.cn

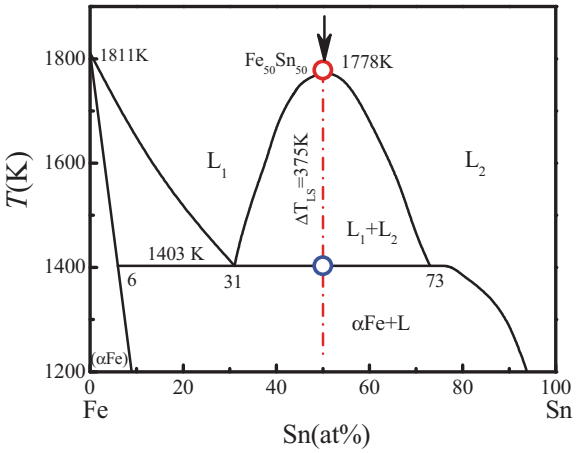

FIG. 1. Binary $Fe_{50}Sn_{50}$ alloy located in the Fe-Sn phase diagram.

Figure 2 shows the homogeneous patterns of binary $Fe_{50}Sn_{50}$ alloy droplets under a free fall condition. For the smallest droplets with diameters less than 83 μm, the macrostructure displays two homogeneous morphologies: One is that phase separation takes place and generates the globular Fe-rich phase distributed into the Sn-rich base phase and the other is that phase separation does not occur and it displays the refined αFe dendritic grown uniformly in the Sn-rich phase as shown in Figs. 2(a)–2(c). According to the binary Fe-Sn diagram in Fig. 1, the phase separation could not occur if the undercooling is larger than the temperature internal of phase separation ($\Delta T > \Delta T_{LS}$), and the αFe phase grows directly from the liquid phase, that is, $L \rightarrow \alpha\mathrm{Fe} + L_2$. In addition, the cooling rate of the 79 μm droplet diameter is up to $1.05 \times 10^5\,\mathrm{K\,s^{-1}}$, which is the highest cooling rate for the experimental result. Because of such high undercooling and cooling rates, the phase separation is suppressed and forms a refined αFe dendritic structure grown in the Sn-rich phase, which is seen in Fig. 2(b). With the increase in droplet diameter, the undercooling and cooling rates decrease. When the droplet diameter is 83 μm, the cooling rate is $9.67 \times 10^4\,\mathrm{K\,s^{-1}}$, here the undercooling enters into the phase separation zone $\Delta T \leqslant \Delta T_{LS}$, and the homogeneous liquid phase begins to take place in phase separation $L \rightarrow L_1 + L_2$. However, the Fe-rich globules do not have enough time to assemble together in the process of liquid phase separation due to the higher cooling rate, and finally it forms the dispersive structure of a globular Fe-rich phase distributed into a Sn-rich base phase as shown in Fig. 2(a). It is clear that the undercooling and cooling rates have a significant influence on the process of phase separation.

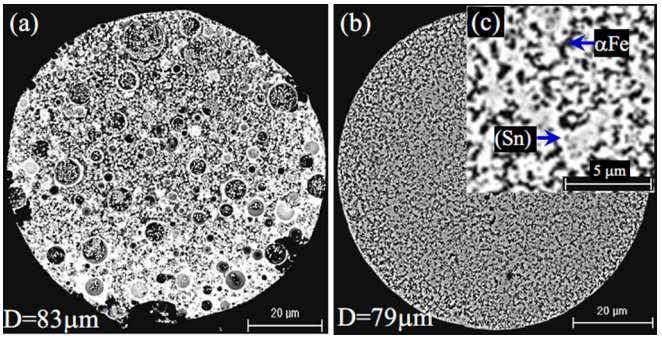

FIG. 2. Rapidly solidified homogeneous structures of a $Fe_{50}Sn_{50}$ alloy, (a) uniform phase separation structure, (b) refined dendritic structure, and (c) a magnified view of the microstructures.

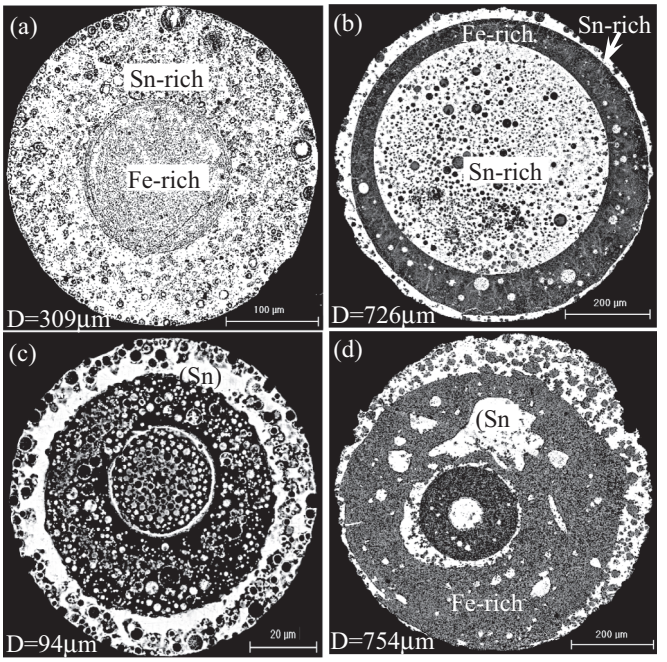

FIG. 3. Typical macrosegregated structures of the $Fe_{50}Sn_{50}$ alloy: (a)–(d) two- to five-layer core-shell structures.

Once the droplet diameter exceeds 83 μm, the undercooling enters completely into the temperature interval of phase separation, that is, $\Delta T < \Delta T_{LS}$, and the cooling rate also decreases. Therefore, a conspicuous liquid phase separation of the binary $Fe_{50}Sn_{50}$ alloy droplet has occurred and formed the special morphologies: two- to five-layer core-shell structures since the smaller undercooling and lower cooling rates. EDS results reveal that the dark zone is the Fe-rich phase, whereas the white zone is the Sn-rich phase. The Sn-rich phase always forms on the droplet surface layer as seen in Fig. 3. It is evident from Fig. 3 that the formations of multilayer macrostructural patterns do not change with the droplet diameter, and every droplet diameter can form the multilayer structure. Meanwhile, it is found that the two-layer core-shell structure is the universal morphology during the experiment, which is deduced to be the most stable morphology in the process of the phase separation.

B. Three dimensional phase field simulation

In order to investigate the phase separation characteristics, the phase field method is employed to simulate the evolution process of the second liquid phase during the phase separation. Based on the modified Model H [18,19], the phase field governing equation is expressed as

$$\frac{\partial \varphi}{\partial \tau} + \nabla \cdot (\boldsymbol{v}\varphi) = \nabla \cdot \left[\varphi(1-\varphi) \nabla \frac{\delta F}{\delta \varphi} \right] + \nabla \cdot \boldsymbol{\xi}, \qquad (1)$$

where φ denotes the molar fraction of the alloy component, τ is the dimensionless time, v is the local velocity, ξ is the

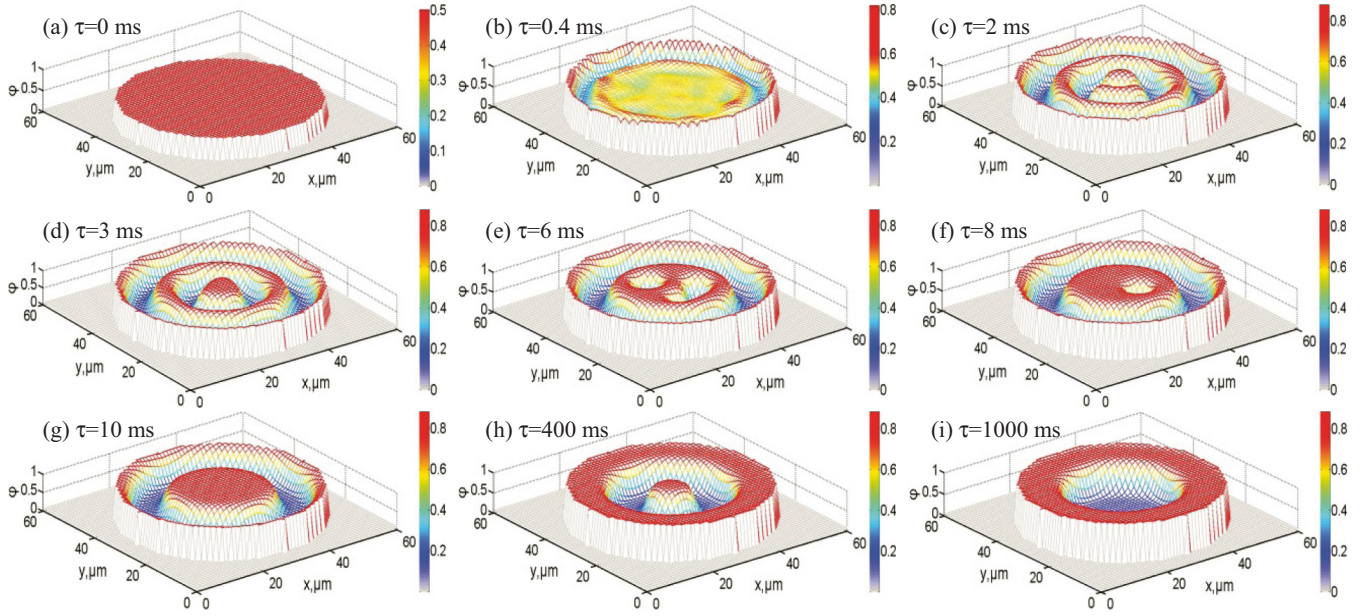

FIG. 4. Three dimensional snapshots of the phase separation process and core-shell structure evolution at different moments: (a)–(f) correspond to the different moments $\tau = 0$–1000 ms.

random Gaussian white noise with the fluctuation amplitude ε. F is the free energy function, which is written as

$$F = F_b + F_{\text{grad}} + F_S, \tag{2}$$

where F_b is the bulk free energy, F_{grad} is the free energy of the concentration gradient, F_S is the surface free energy, which plays a crucial role in phase separation. F_b is given as

$$F_b = \int \{F_{b0} + \theta[\varphi \ \ln \ \varphi + (1-\varphi)\ln(1-\varphi)] + 2\varphi(1-\varphi)\}dV, \tag{3}$$

where F_{b0} is the constant part and θ is the reduced temperature. F_{grad} is expressed by

$$F_{\text{grad}} = \frac{1}{2}\int (\nabla\varphi)^2 dV. \tag{4}$$

F_S is taken as

$$F_S = F_{S0} - H\varphi_S + \tfrac{1}{2}g\varphi_S^2, \tag{5}$$

where φ_S represents the surface concentration and F_{S0}, H, and g are constants describing the surface preferential attraction properties.

In small droplets, the Reynolds number is less than the magnitude of 10^{-3}, thus the local velocity can be expressed by [24]

$$\boldsymbol{v} = -C_f\varphi\nabla\mu, \tag{6}$$

where C_f is the fluidity parameter of the alloy melt, which is the ratio between thermal and viscous forces [25,26]. It is expressed as

$$C_f = \frac{\rho R_g T_c \varepsilon^2}{6\pi D_L \eta M}, \tag{7}$$

where ρ is the density of the liquid alloy, R_g is the gas constant, ε is the length scale, D_L is the diffusion coefficient, η is the viscosity, and M is the molar weight.

During phase field simulation, the initial fluid velocity is zero. The grid size is set as $\Delta x = \Delta y = 1$ with a fixed lattice size of $R_0 = 100$. The time step $\Delta\tau = 0.001$ ensures the stability of a numerical solution. The surface parameters are $H = 0.35$ and $g = 0.4$. The calculations were performed in a Lenovo 1800 cluster system.

The 3D microstructural evolution snapshots from the phase field simulation of the binary $Fe_{50}Sn_{50}$ alloy at different moments are shown in Fig. 4. At the beginning of phase separation, the concentration of the liquid alloy remains homogeneous ($\tau = 0$) as shown in Fig. 4(a). With the evolutionary time extension, the hydrodynamic effect begins to appear visibly, the phase separation occurs, and the liquid morphology varies with the evolutionary time of phase separation. The Sn-rich globules aggregate together, a part of the Fe-rich liquid phase is stuck in the middle of the Sn-rich liquid phase, and the liquid $Fe_{50}Sn_{50}$ alloy forms a three-layer multilayer structure when the evolutionary time is $\tau = 0.4$ ms. Here the red phases are the Sn-rich liquid phase, and the blue phases are the Fe-rich liquid phase. Under the effects of the hydrodynamic and Marangoni migrations, the liquid phase separation becomes much faster, and the five-layer multilayer structure appears at $\tau = 3$ ms, which is shown in Fig. 4(d). As the phase separation time extends, the Sn-rich phase coagulates again, and the layer number of the multilayers decreases gradually. Finally the two-layer core-shell structure forms in the liquid phase in the process of phase separation as illustrated in Figs. 4(e)–4(i). Obviously, the simulated structures are in accordance with the experimental results, which indicate that the modified Model H can reasonably describe the morphological evolution of the $Fe_{50}Sn_{50}$ alloy under free fall conditions. According to the above analysis, the shortest phase separation time, largest undercooling, and highest cooling rate

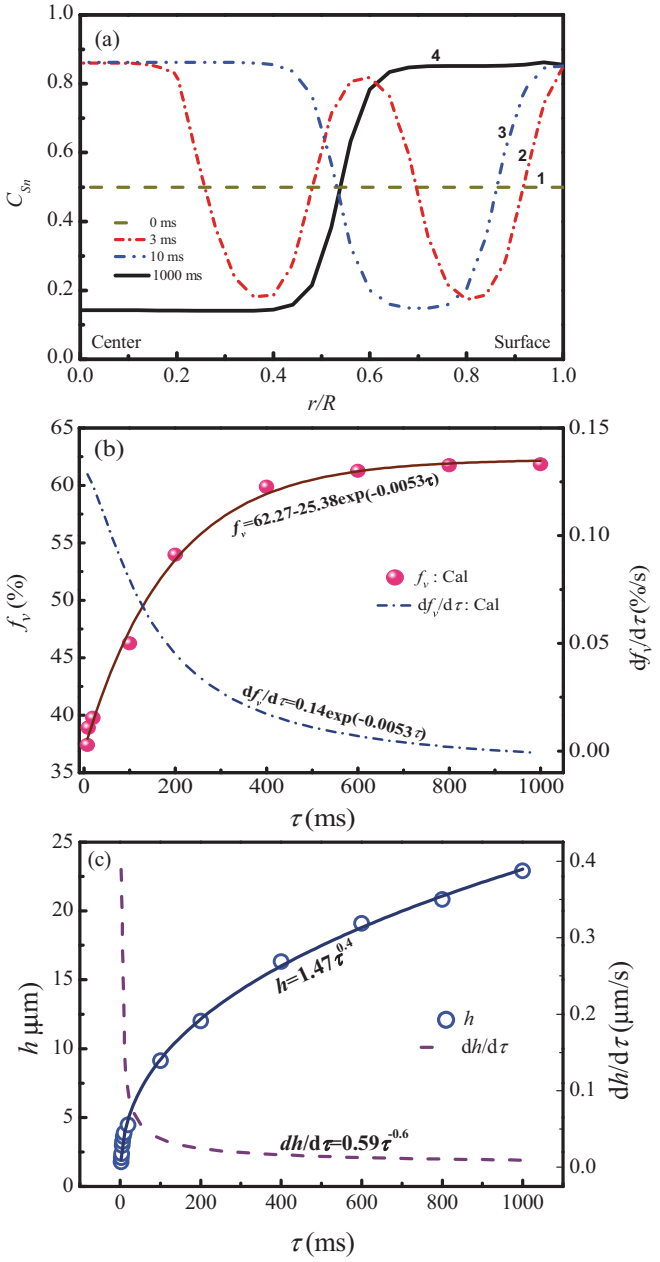

FIG. 5. Radial concentration distribution and evolution parameters of the Sn-rich phase at different moments in the alloy droplet, (a) radial concentration distribution of the Sn solute, (b) volume fraction and increasing rate, and (c) surface segregation layer thickness and increasing rate.

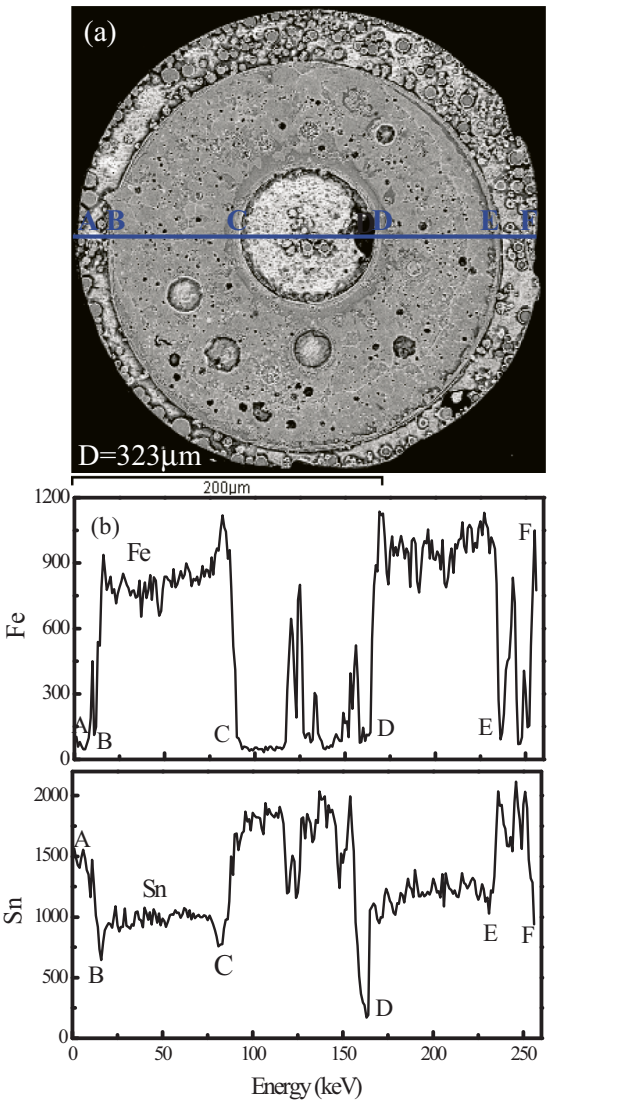

FIG. 6. Solute distribution of a three-layer core-shell structure: (a) EDS scanning line, (b) profile of the Fe content, and (c) profile of the Sn content.

are the main reasons for the homogeneous patterns as seen in Figs. 1, 2, and 4. In addition, the longer phase separation time, smaller undercooling, and lower cooling rate lead to multilayer structures. Apparently, the two-layer core-shell structure is the ultimate and stable structure for the monotectic alloy during the phase separation as shown in Fig. 4(i).

In order to explore the influences of surface segregation and Marangoni migration on the concentration field during phase separation, the radial distribution of the Sn solute at various moments is illustrated in Fig. 5. Clearly, the radius concentration distribution fluctuates with reduced radius r/R. Before the occurrence of phase separation, the concentration profile displays an almost straight line, which represents the homogenous liquid phase ($\tau = 0$ ms). With the extension of evolutionary time, the Sn-rich liquid phase fluctuates drastically and gathers together rapidly; it forms a five-layer multilayer structure due to the effect of surface layer segregation ($\tau = 3$ ms). As the phase separation continues, the outer Sn-rich layer thickens rapidly, the inner Sn-rich liquid aggregates together, and the triple-layer structure is formed ($\tau = 10$ ms). Under the influence of Marangoni migration and surface segregation, the surface layer thickens gradually, and in contrast the central Sn-rich area reduces rapidly, eventually resulting in the formation of a two-layer core-shell structure ($\tau = 1000$ ms). Figure 6 presents the EDS analysis results of the solute profiles along a radial line for the three-layer core-shell structure formed in a 323 μm diameter alloy droplet. It is evident that the distribution characteristics of Sn and Fe in Figs. 6(b) and 6(c) agree well with the numerically simulated concentration field in Fig. 5(a) at the moment $\tau = 10$ ms. Consequently there is not sufficient time for the complete

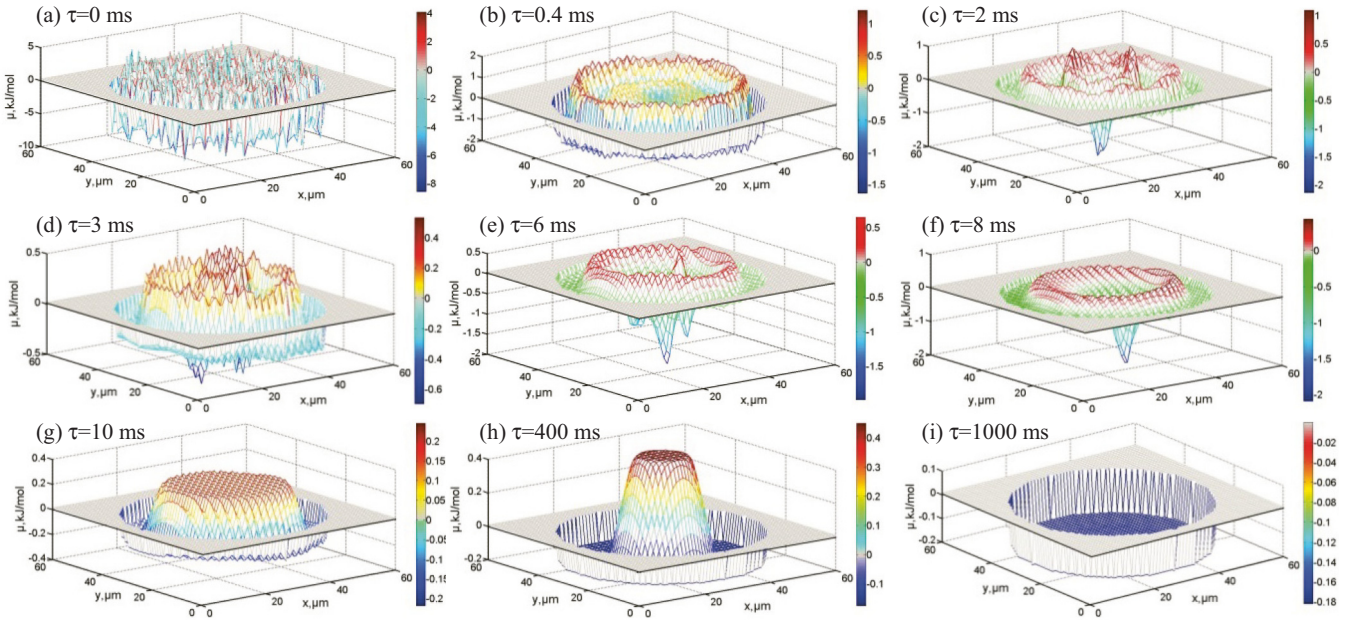

FIG. 7. Chemical potential profile versus evolution moments: (a)–(i) correspond to the different moments $\tau = 0$, 0.4, 2, 3, 6, 8, 10, 400, and 1000 ms.

evolution of a multilayer structure in this case, which manifests the metastable characteristics. The above analysis provides a more useful situation to reveal the actual concentration field in the intermediate stage of liquid phase separation.

The volume fraction of the Sn-rich phase and its increase rate can be used to describe the evolution feature in the process of phase separation. The volume fraction displays the increase tendency as evolutionary time extends as shown in Fig. 5(b). The volume fraction increases rapidly when the evolutionary time is lower than 400 ms. Once the evolutionary time is longer than 400 ms, the volume fraction begins to flatten. The increase rate of the volume fraction demonstrates the reverse trend as compared with the volume fraction. As the evolutionary time is shorter than 400 ms and the increase rate decreases quickly, it then reduces slowly when $\tau > 400$ ms. The surface segregation layer thickness and its increase rate are illustrated in Fig. 5(c). Similarly, the Sn-rich globules gather rapidly which leads to the fact that the thickness of the outer Sn-rich layer thickens dramatically in the period of phase separation as $\tau \leqslant 400$ ms, thus it forms a metastable multilayer structure. Then the thickness of the outer Sn-rich layer thickens slowly, its increase rate reduces gradually, and the layer number of the core-shell structure decreases at the same time with the extension of evolutionary time. Obviously, the Sn-rich globules inside the liquid phase move rapidly in the initial stage of phase separation and form a multilayer structure when $\tau \leqslant 400$ ms, then the Ostwald ripening plays an important role once $\tau > 400$ ms, and the phase separation gradually stabilizes and forms the two-layer core-shell structure at the end of the phase separation. This is further proof that the two-layer core-shell structure is the most stable morphology during the phase separation for the monotectic alloy.

The chemical potential represents the system stability feature during the phase separation. As shown in Fig. 7(a), the chemical potential of the liquid alloy distributes disorderly, the maximum absolute value attains about 3.38 kJ mol^{-1} before the occurrence of phase separation, and the liquid phase displays the extremely unstable condition. With the development of phase separation, the maximum value decreases gradually, and the positive value of the chemical potential decreases to 1.45 kJ mol^{-1} at the evolution time of $\tau = 0.4$ ms, which is seen in Fig. 7(b). When the evolution time extends to 10 ms, the thickness of the outer chemical potential layer thickens distinctly since it absorbs the liquid energy of the Sn-rich chemical potential around itself, the inner chemical potential also appears as a visible peak, and the positive value of the chemical potential reduces to 0.1 kJ mol^{-1} with the decrease in the system Gibbs active energy, which is shown in Fig. 7(g). However, the area of the inner chemical potential reduces gradually, but the energy increases remarkably, and the maximum chemical potential attains about 0.3 kJ mol^{-1} when the evolution time is $\tau = 400$ ms. The reason is that the inner chemical potential absorbs a large amount of energy from the liquid phase, which enhances notably the positive value of the chemical potential. Furthermore, the inner chemical potential disappears completely, it presents a hole feature at $\tau = 1000$ ms, the value of the chemical potential shows the whole negative value, and the minimum value is only -0.18 kJ mol^{-1} as seen in Fig. 7(i). Obviously, the system acquires the absolutely stable condition when the evolution time is long enough and the phase separation process tends to slow down from the evolution characteristics of system potential. It is furthermore demonstrated that the two-layer structure, which forms an easy morphology in the process of phase separation, is the most stable.

C. Fluid dynamics inside freely falling alloy droplets

The gravitational acceleration has been reduced to $10^{-3}g_0$ in the drop tube experiment, a great amount of experimental results manifest that the Stokes motion velocity is far less

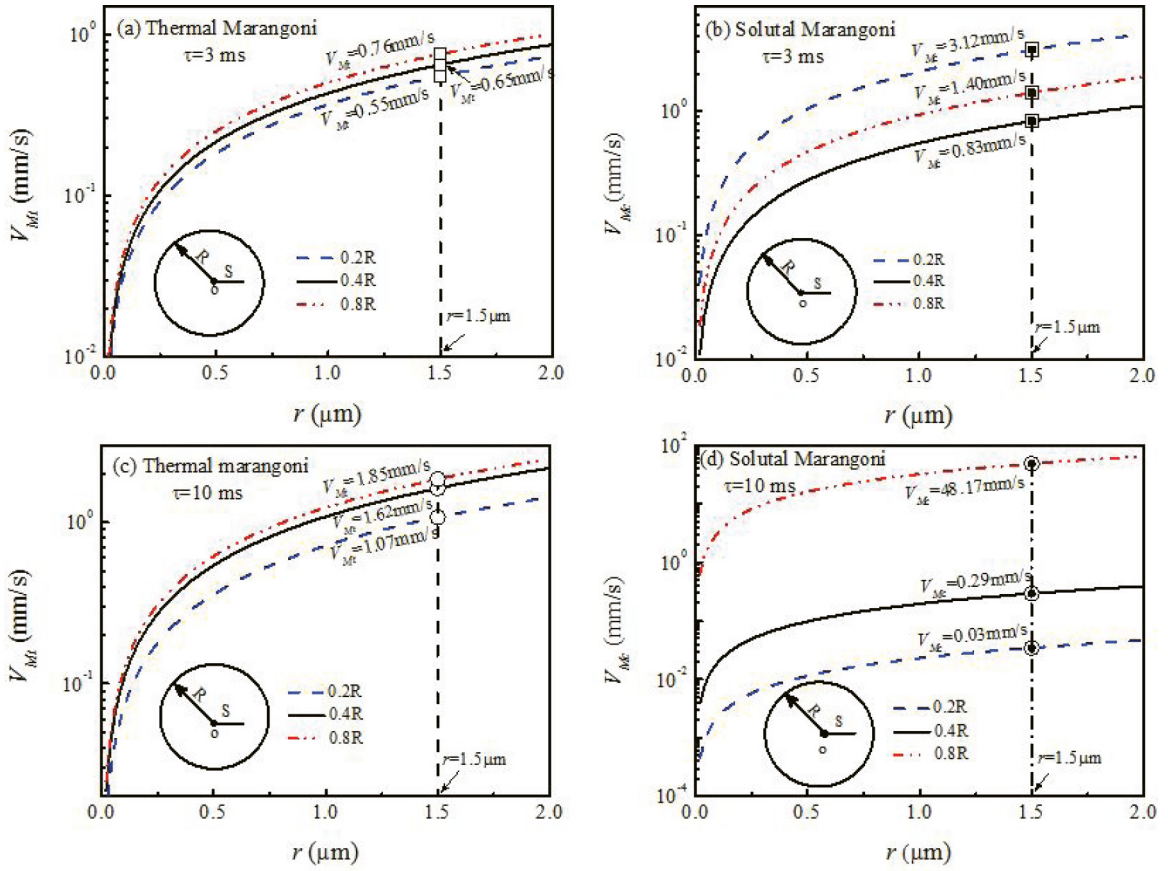

FIG. 8. Thermal and solutal Marangoni migration velocities versus droplet radius, (a) and (b) thermal and solutal Marangoni migration at $\tau = 3$ ms and (c) and (d) thermal and solutal Marangoni migration at $\tau = 10$ ms.

than the thermal and solutal Marangoni migration velocities [7,17,18,20,21], it has an insignificant effect during the phase separation, and therefore the Stokes motion can be neglected under the free fall condition. Marangoni migration was calculated to reveal the kinematic mechanisms of dispersed globules in the process of phase separation. The actual movement of the Sn-rich globule is determined by the superposition of two types of motion: thermal Marangoni migration and solutal Marangoni migration in the reduced gravity condition. The thermal Marangoni migration impels the globules to move inwards to the droplet center because the interfacial tension between the liquid Fe-rich and the Sn-rich phase increases with the decrease in internal temperature. Meanwhile, the concentration gradients tend to push the globules to move outwards from the droplet surface under the effect of the solutal Marangoni migration [27–29]. The thermal Marangoni migration velocity V_{Mt} of a Sn-rich globule can be expressed as

$$V_{Mt} = -\frac{2k_1 \nabla\sigma_t}{(2k_1 + k_2)(2\eta_1 + 3\eta_3)} r, \tag{8}$$

$$\nabla\sigma_t = \frac{\partial\sigma}{\partial T}\frac{\partial T}{\partial r}. \tag{9}$$

Here $\nabla\sigma_t$ is the interfacial tension gradient resulting from the temperature field, and $\partial\sigma/\partial T$ represents the temperature-dependent coefficient of the interfacial tension. k_1 and k_2 are the thermal conductivities of the matrix and the dispersive phases, and η_1 and η_2 are their viscosities, respectively. $\partial T/\partial r$ stands for the temperature gradient of the alloy droplet.

Meanwhile, the solutal Marangoni migration should be taken into account during phase separation owing to the evaluation and modulation of the concentration field [21,29].The solutal Marangoni migration velocity of the Sn-rich globules is written by

$$V_{Mc} = -\frac{2D_1 \nabla\sigma_c}{(2D_1 + D_2)(2\eta_1 + 3\eta_2)} r, \tag{10}$$

$$\nabla\sigma_c = \frac{\partial\sigma}{\partial C}\frac{\partial C}{\partial r}. \tag{11}$$

$\nabla\sigma_c$ is the interfacial tension gradient caused by the concentration field, D_1 and D_2 are the solutal diffusion coefficients of the matrix and dispersive phases, and $\partial\sigma/\partial c$ is the concentration-dependent coefficient of the interfacial tension. $\partial C/\partial r$ represents the concentration gradient.

Based on Eqs. (8)–(11), the thermal and solutal Marangoni migration velocities at different globule radii, sites, and moments have been calculated, and the results are shown in Fig. 8. Here r is a globule radius inside a droplet, R represents a droplet radius, and S is the distance from the droplet center. At the initial stage ($\tau = 3$ ms), the liquid phase is at the metastable condition, the microstructure shows the five-layer core-shell feature, the globule radius is small, and the thermal Marangoni migration velocity (V_{Mt}) is slow similarly as seen in Fig. 8(a). The globules near the alloy droplet surface have the large

thermal Marangoni migration velocity. For example, the Sn globules with radii of 1.5 μm show a thermal Marangoni migration velocity of 0.76 mm s^{-1} at $S = 0.8R$, which is larger than that of $S = 0.2R$ where the Sn-rich globule shows a thermal Marangoni migration velocity of 0.55 mm s^{-1}. When the evolution time extends to 10 ms, the globules grow up rapidly, and the thermal Marangoni migration velocity increases simultaneously, which is illustrated in Fig. 8(c). For $S = 0.8R$, the thermal Marangoni migration velocity V_{Mt} is 1.85 mm s^{-1} where the globule radius r is 1.5 μm, which is about 1.7 times larger than that of the site $S = 0.2R$ where the thermal Marangoni migration velocity is 1.07 mm s for the same radius. Obviously, the larger globules have the larger thermal Marangoni velocity as seen in Figs. 8(a) and 8(c), and the large globules near the droplet surface have the large thermal Marangoni migration velocity, which drives the globules to move rapidly inwards to the droplet center under the effect of the temperature field.

The solutal Marangoni migration velocity displays different tendencies, which can be seen in Figs. 8(b) and 8(d). At the evolution moment of $\tau = 3$ ms, the globules near the center ($S = 0.2R$) and the surface ($S = 0.8R$) show the large solutal Marangoni migration velocity, and the velocity of the center globules are 2.2 times larger than the surface globules when the globule radius r is 1.5 μm, which leads to a large number of globules moving outwards from the surface under the effect of the concentration field. However, the solutal Marangoni migration velocity near the droplet surface ($S = 0.8R$) increases when the evolution time extends to 10 ms, $V_{Mc} = 48.17$ mm s^{-1}, which is considerably larger than the center globules ($S = 0.2R$) where the velocity is only 0.03 mm s^{-1}. Obviously, the globules near the droplet surface have large solutal Marangoni velocities when the evolution time is 10 ms, and a great quantity of globules moves rapidly outwards from the surface and forms the three-layer core-shell structure. With the extension of time, the center globules move to the surface under the effect of solutal Marangoni convection, and a two-layer core-shell structure forms in the liquid phase. Besides, the solutal Marangoni migration velocity at the center and near the droplet surface changes remarkably with the evolution time, which is an important factor for the formation of the multilayer core-shell structure during phase separation. Clearly, the solutal Marangoni migration is more complex than the thermal Marangoni migration during the phase separation for the binary $Fe_{50}Sn_{50}$ alloy.

According to the above analysis, the final structures are controlled by the Marangoni migration velocity, evolution time, and chemical potential stability. The solutal Marangoni migration plays a greater role during phase separation because the solutal Marangoni migration velocity is larger than the thermal Marangoni migration velocity with the extension of the evolution time. In addition, the longer the evolution time, the faster the solutal Marangoni migration velocity, and the more stable the chemical potential. As a consequence, a large number of Sn-rich liquid globules move toward the droplet surface under the effect of solutal Marangoni migration, and a two-layer core-shell structure ultimately is formed in the liquid phase.

IV. CONCLUSIONS

To summarize, the binary $Fe_{50}Sn_{50}$ immiscible alloy was rapidly solidified under the containerless free falling conditions within a drop tube. Three dimensional phase field simulation and fluid dynamics analysis were both accomplished to reveal its microstructure evolution process. The main findings include the following aspects:

(1) The containerless microgravity solidification results in three types of microstructures: homogeneous dendrites, uniform dispersions, and multilayer core-shells. Scanning electron microscopy analyses indicate that two- to five-layer core-shell structures are the dominant morphologies. Dendritic microstructures were formed only when the undercooling and cooling rates are high enough to suppress liquid phase separation.

(2) The 3D dynamic phase field simulation demonstrates that the uniformly dispersive structure and the three- to five-layer core-shells are all metastable transitional states of the liquid phase separation process. Whereas the two-layer core-shell structure is the most stable morphology with the lowest chemical potential.

(3) Because Stokes motion is effectively prevented by the microgravity condition in the drop tube, the two types of Marangoni migrations play the dominating role in the evolution of macrosegregated structures. In comparison, the solutal Marangoni migration velocity is always larger than the thermal Marangoni migration velocity. Thus the surface segregation and solutal Marangoni migration are the controlling factors for multilayer core-shell structures.

ACKNOWLEDGMENTS

The authors are grateful to Dr. F. P. Dai and Dr. B. C. Luo for their help with the experiments. Financial support from the National Natural Science Foundation of China (Grants No. 51371150, No. 51271150, No. 51327901, and No. 51571163) is acknowledged with gratitude.

[1] D. Miyajima *et al.*, Science **336**, 209 (2012).
[2] Q. Zhang, I. Lee, J. B. Joo, F. Zaera, and Y. D. Yin, Acc. Chem. Res. **46**, 1816 (2013).
[3] C. D. Keating, Acc. Chem. Res. **45**, 2114 (2012).
[4] S. Thakur, P. A. Pullarkat, and P. B. S. Kumar, Phys. Rev. E **80**, 011708 (2009).
[5] D. M. Li, W. B. Krantz, A. R. Greenberg, and R. L. Sani, J. Membr. Sci. **279**, 50 (2006).
[6] I. Karban, S. Curiotto, D. Chatain, and W. Hoyer, Acta Mater. **58**, 3406 (2010).
[7] W. L. Wang, X. M. Zhang, L. H. Li, and B. Wei, Sci China: Phys., Mech. Astron. **55**, 450 (2012).
[8] R. Monti, R. Savino, and G. Alterio, Acta Astronaut. **51**, 789 (2002).
[9] I. Yamauchi, T. Irie, and H. Sakaguchi, J. Alloys Compd. **51**, 789 (2002).

[10] D. Mirkovic, J. Gröbner, and R. Schmid-Fetzer, Acta Mater. **56**, 5214 (2008).
[11] W. L. Wang, X. M. Zhang, H. Y. Qin, and B. Wei, Philos. Mag. Lett. **89**, 683 (2009).
[12] S. Yaneva *et al.*, Mater. Sci. Eng., A **515**, 59 (2009).
[13] I. G. Kaban and W. Hoyer, Phys. Rev. B **77**, 125426 (2008).
[14] H. Neumann, Y. Plevachuk, and F. Allenstein, Mater. Sci. Eng., A **361**, 155 (2003).
[15] S. Ozawa and T. Motegi, Mater. Lett. **58**, 2548 (2004).
[16] K. Tafa, S. Puri, and D. Kumar, Phys. Rev. E **64**, 056139 (2001).
[17] T. Qin, H. P. Wang, and B. Wei, Sci. China, Ser. G: Phys., Mech. Astron. **50**, 546 (2007).
[18] B. C. Luo, X R. Liu, and B. Wei, J. Appl. Phys. **106**, 053523 (2009).
[19] H. Tanaka, J. Phys.: Condens. Matter **13**, 4637 (2001).
[20] Y. H. Wu, W. L. Wang, Z. C. Xia, and B. Wei, Comput. Mater. Sci. **103**, 179 (2015).
[21] W. L. Wang, Z. Q. Li, and B. Wei, Acta Mater. **59**, 5482 (2011).
[22] H. Minakuchi, Y. Takagi, Y. Okano, S. Gima, and S. Dost, J. Cryst. Growth **385**, 61 (2014).
[23] T. B. Massalski, J. L. Murray, L. H. Bennett, and H. Baker, ASM Int. **1**, 1774 (1986).
[24] N. M. Mautits, A. V. Zvelindovsky, G. J. Sevink *et al.*, J. Chem. Phys. **108**, 9150 (1998).
[25] H. Tanaka and T. Araki, Phys. Rev. Lett. **81**, 389 (1998).
[26] N. Vladimirova, A. Malagoli and R. Mauri, Phys. Rev. E **60**, 6968 (1999).
[27] P. L. Schaffer, R. H. Mathiesen, and L. Arnberg, Acta Mater. **57**, 2887 (2009).
[28] S. Thakur, P. B. S. Kumar, N. V. Madhusudana, and P. A. Pullarkat, Phys. Rev. Lett. **97**, 115701 (2006).
[29] V. G. Karpov and D. W. Oxtoby, Phys. Rev. E **55**, 7253 (1997).